Supporting Information

Electrochemiluminescence of a Novel Iridium(III) Complex with Dual-Potential Emission and Its Sensing for Chloramphenicol

Tongtong Li,[a] Yingying Su,[b] Mingxia Sun,[b] Hongjie Song,*[a] and Yi Lv[a b]

a. Key Laboratory of Green Chemistry and Technology of Ministry of Education, College of Chemistry, Sichuan University, 29 Wangjiang Road, Chengdu 610064, P. R. China. E-mail: lvy@scu.edu.cn.

b. Analytical & Testing Center, Sichuan University, Chengdu 610064, P. R. China.

Corresponding author: songhj@scu.edu.cn, lvy@scu.edu.cn

Table of Contents

1. Experimental Section

1.1 Chemicals and Reagents.

2-bromoquinoline, benzo[b]thien-2-ylboronic acid, dichloromethane (DCM), 2-ethoxyethanol, [2,2'-bipyridine]-4,4'-dicarboxylic acid, 2,2'-bipyridine, 1,10-phenanthroline, Nafion solution (5 wt%), anhydrous sodium sulfate (Na_2SO_4), [1,1'-bis(diphenylphosphino)ferrocene]dichloropalladium(II) ($Pd(dppf)Cl_2$), N, N-dibutylethanolamine (DBAE), N, N-diethylethanolamine (DEEA), N, N-dimethylaminoethanol (DMEA), N, N-diisopropylethylamine (DIPEA), sodium citrate, sodium dihydrogen phosphate dihydrate ($NaH_2PO_4\cdot 2H_2O$) and disodium hydrogen phosphate dodecahydrate ($Na_2HPO_4\cdot 12H_2O$) were obtained from Titan Scientific Co., Ltd. (Shanghai, China). Methanol (MeOH), ethanol (EtOH), hydrazinium hydrate ($N_2H_4\cdot H_2O$), tri-n-propylamine (TPA), triethylamine (TEA) and trimethylamine (TMA) were purchased from Aladdin Biochemical Technology Co., Ltd. (Shanghai, China). Chloro-auric acid tetrahydrate ($HAuCl_4\cdot 4H_2O$) and tris(2,2'-bipyridyl) dichlororuthenium(II) hexahydrate ($Ru(bpy)_3^{2+}$) were obtained from Merck Ltd. Potassium carbonate (K_2CO_3), potassium persulfate ($K_2S_2O_8$), potassium chloride (KCl) were acquired from Kelong Chemical Co., Ltd. (Chengdu, China) and potassium ferricyanide ($K_3[Fe(CN)_6]$), potassium ferrocyanide ($K_4[Fe(CN)_6]$), sodium oxalate ($Na_2C_2O_4$) were purchased from Kermel Chemical Reagent Co., Ltd. (Tianjin, China). $IrCl_3\cdot 3H_2O$ was obtained from Bide Pharmatech Co., Ltd. (Shanghai, China). Single-walled carbon nanotubes (SWCNTs) were acquired from Xianfeng Nanomaterials Technology Co., Ltd. (Jiangsu, China). Chloramphenicol (CAP), kanamycin sulfate (KAN), gentamycin sulfate (GEN), ampicillin sodium (AMP), streptomycin (STR), tetracycline hydrochloride (TC) and oxytetracycline (OTC) were obtained from Macklin Biochemical Co., Ltd. (Shanghai, China). All the chemical agents were of analytical grade or better and used as received from the indicated suppliers without secondary purification, and all aqueous solutions were prepared using ultrapure water (resistivity of 18.25 $M\Omega\cdot cm$).

1.2 Apparatus and Instruments.

^{1}H NMR and ^{13}C NMR spectra were determined by 400 MHz and 101 MHz using Bruker Avance II-400 NMR spectrometer (Germany). High-resolution mass spectra (HRMS) were obtained using an ESI ionization source on a Q Exactive Plus Orbitrap Mass Spectrometer (Thermo Scientific, Bremen, Germany). Morphological features of materials were examined via transmission electron microscopy (TEM, Tecnai G2 F20, USA) and scanning electron microscopy (SEM-S3400, Hitachi, Japan), while the elemental distribution of the material was analyzed using energy-dispersive X-ray spectroscopy (EDS) coupling SEM and diameter distribution of nanoparticles was calculated using Nano Measurer (1.2 version). Zeta potential were operated by Malvern Zetasizer Nano ZS90 (Malvern PANalytical Ltd., Shanghai, China). The fluorescence spectra measurements were performed on a Hitachi F-7000 spectrophotometer (Japan) and UV-Vis absorption spectra were measured on a Hitachi U-2910 spectrophotometer (Japan). The ECL signal was measured on a model BPCL-ECL 150 electrochemiluminescence analyzer (Guangzhou Microphonic Technology Co., Ltd., China). The cyclic voltammetric (CV) and electrochemical impedance spectroscopy (EIS) were performed with a CHI660E electrochemistry workstation (Shanghai Chenhua Instruments, China). Fourier-transform infrared (FT-IR) spectra were recorded using a Invenio R spectrometer (Bruker, Germany) in the wavenumber range of 400-4000 cm^{-1}. The photoluminescence absolute quantum yields (PLQY, ΦPL) were obtained by a Quantaurus-QY Plus U spectrometer (HAMAMATSU, Japan).

1.3 Synthesis and Characterization of Ir-based Complexes.

(1) Synthesis of C^N main ligand btiq.

Compound btiq was synthesized by Suzuki coupling reaction[1]. Specifically, 2-Bromoquinoline (412 mg, 2 mmol), Benzo[b]thien-2-ylboronic acid (356 mg, 2 mmol) and catalyst Pd(dppf)Cl_2 (180 mg, 0.25 mmol) were added into a flask containing 20 mL dioxane, after ultrasonic dispersion, K_2CO_3 (1g in 3 mL water) was added and the mixture was heated to 80°C with stirring for 24 hours under a nitrogen atmosphere. After the reaction was cooled to room temperature, the crude product was extracted with dichloromethane. The obtained organic phase was dried with anhydrous Na_2SO_4 and the organic solvent was removed by rotary evaporation. The crude was purified by column chromatography on silica gel using CH_2Cl_2/MeOH (100:1, v/v) as eluent. The product was a pale-yellow solid and the yield was 64%. ^{1}H NMR (400 MHz, Chloroform-d) δ 8.16 (dd, J = 8.5, 5.5 Hz, 2H), 7.98 (s, 1H), 7.93 – 7.87 (m, 2H), 7.86 – 7.81 (m, 1H), 7.78 (d, J = 8.1 Hz, 1H), 7.73 (ddd, J = 8.4, 6.9, 1.5 Hz, 1H), 7.56 – 7.48 (m, 1H), 7.42 – 7.34 (m, 2H). ^{13}C NMR (101 MHz, Chloroform-d) δ 152.35, 148.13, 145.45, 141.31, 140.58, 136.78, 130.12, 129.51, 127.63, 127.59, 126.70, 125.48, 124.65, 124.46, 122.73, 117.96. HRMS (ESI, m/z): calcd. For $C_{17}H_{11}NS$, 262.0685 $[M+H]^+$; found, 262.0684.

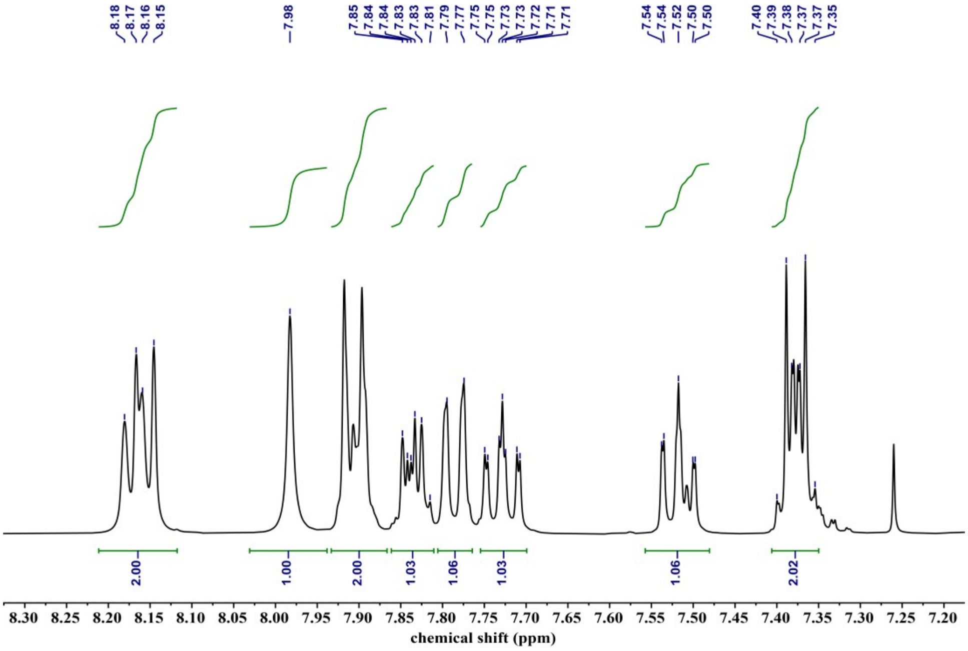

Figure S1. ^{1}H NMR (400 MHz, $CDCl_3$) spectrum of btiq.

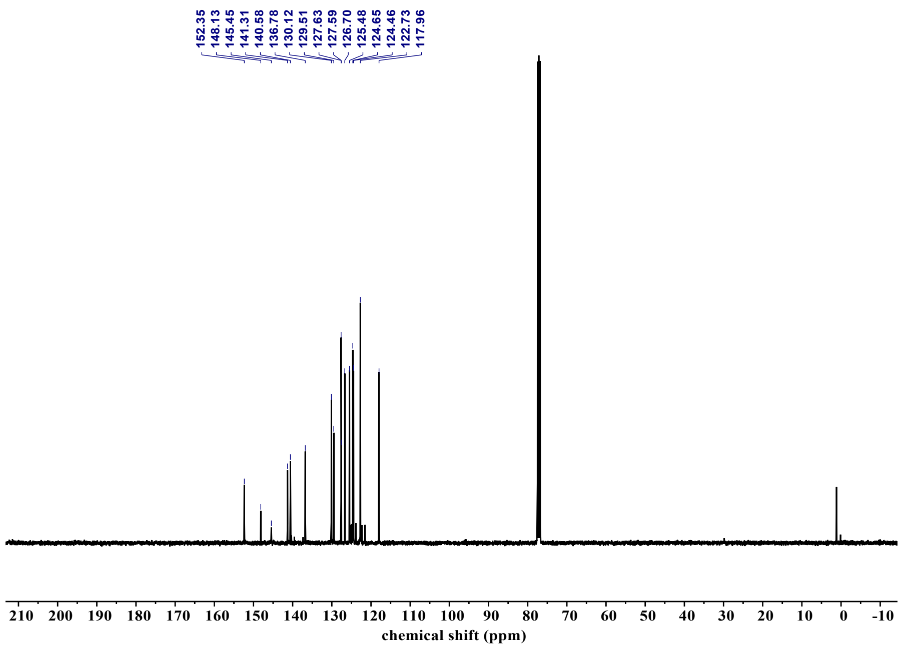

Figure S2. ^{13}C NMR (101 MHz, $CDCl_3$) spectrum of btiq.

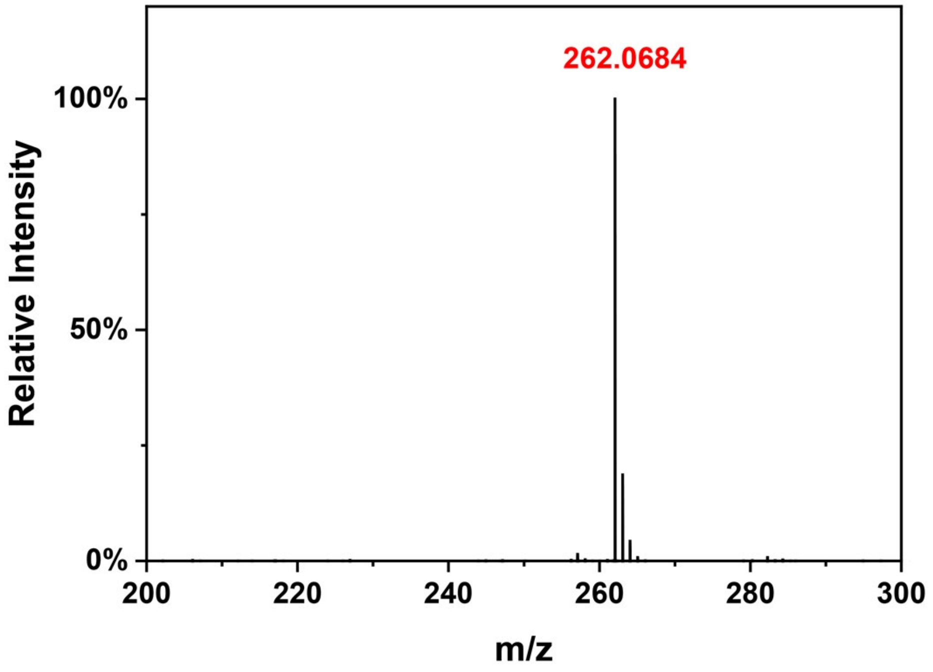

Figure S3. HRMS spectra of btiq.

(2) Synthesis of $[Ir(btiq)_2Cl]_2$.

A mixed solvent of 24 mL 2-ethoxyethanol and water (3:1, v/v) was added to a flask containing $IrCl_3 \cdot 3H_2O$ (352.6 mg, 1 mmol) and C^N ligand btiq (548.8 mg, 2.1 mmol). Subsequently, the mixture was reacted at 115°C for 24 hours under a protective nitrogen atmosphere. After the reaction was completed and cooled to room temperature, 20 mL of ice water was added, and the resulting solid was collected by filtration and washed with cold water and ethanol. The red-brown precipitate was cyclometalated iridium(III) chloro-bridged dimeric intermediate $[Ir(btiq)_2Cl]_2$ and the yield was 89%. The crude product was used in the next reaction without any additional treatment. HRMS (ESI, m/z): 713.06 $[1/2M-Cl^-]^+$.

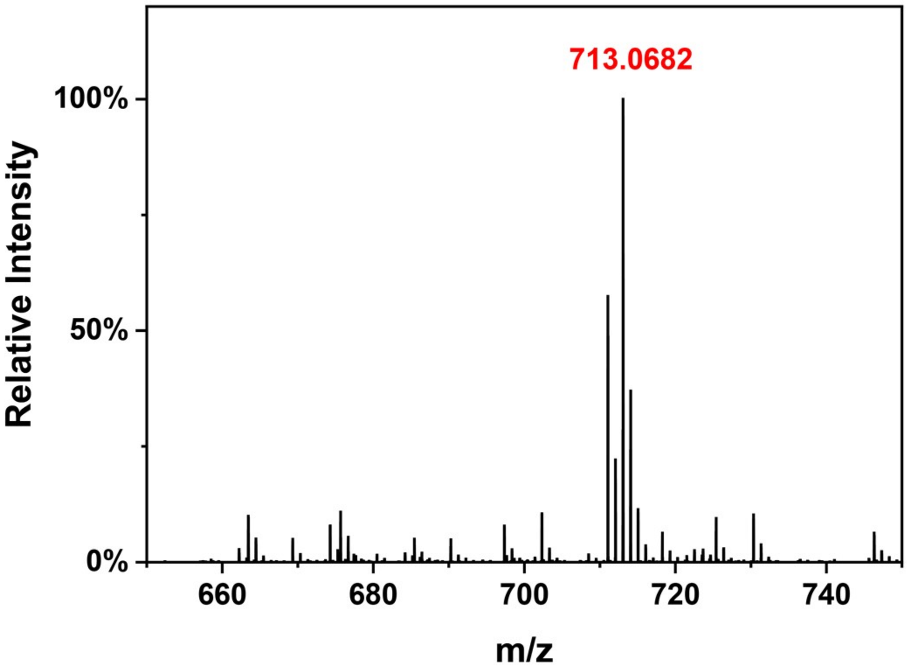

Figure S4. HRMS spectra of $[Ir(btiq)_2Cl]_2$.

(3) Synthesis of probe Ir-COOH, Ir-Bpy and Ir-Phen.

$[Ir(btiq)_2Cl]_2$ (149.9 mg, 0.1 mmol) and [2,2'-bipyridine]-4,4'-dicarboxylic acid (48.8 mg, 0.2 mmol) were combined in a 50 mL flask with 10 mL of a mixed solvent of methanol and dichloromethane (1:1, v/v). The mixture was then heated at 80°C and refluxed overnight under a nitrogen protection. The solvent was efficiently removed via rotary evaporation and purified by silica gel chromatography using CH_2Cl_2/CH_3OH (20:1, v/v) as eluent. The product was dark red, and the yield was 71%.

Ir-COOH: ^1H NMR (400 MHz, DMSO-d6) δ 8.55 (d, J = 8.6 Hz, 2H), 8.28 (d, J = 5.6 Hz, 2H), 8.21 (d, J = 8.5 Hz, 2H), 8.02 (d, J = 8.1 Hz, 2H), 7.94 – 7.89 (m, 4H), 7.33 (t, J = 7.9 Hz, 3H), 7.18 (t, J = 7.5 Hz, 4H), 7.04 (d, J = 8.1 Hz, 3H), 6.97 (d, J = 7.8 Hz, 2H), 6.68 (t, J = 7.7 Hz, 2H), 6.21 (d, J = 8.2 Hz, 2H). ^{13}C NMR (101 MHz, DMSO-d6) δ 166.12, 155.00, 151.33, 147.95, 147.66, 145.93, 142.59, 141.81, 140.49, 139.98, 137.32, 131.26, 129.65, 128.88, 126.84, 126.28, 126.00, 125.24, 124.53, 124.21, 123.51, 122.97, 120.51. HRMS (ESI, m/z): $C_{46}H_{28}IrN_4O_4S_2^+$, 957.1181 [M]$^+$; found, 957.1181 [M]$^+$.

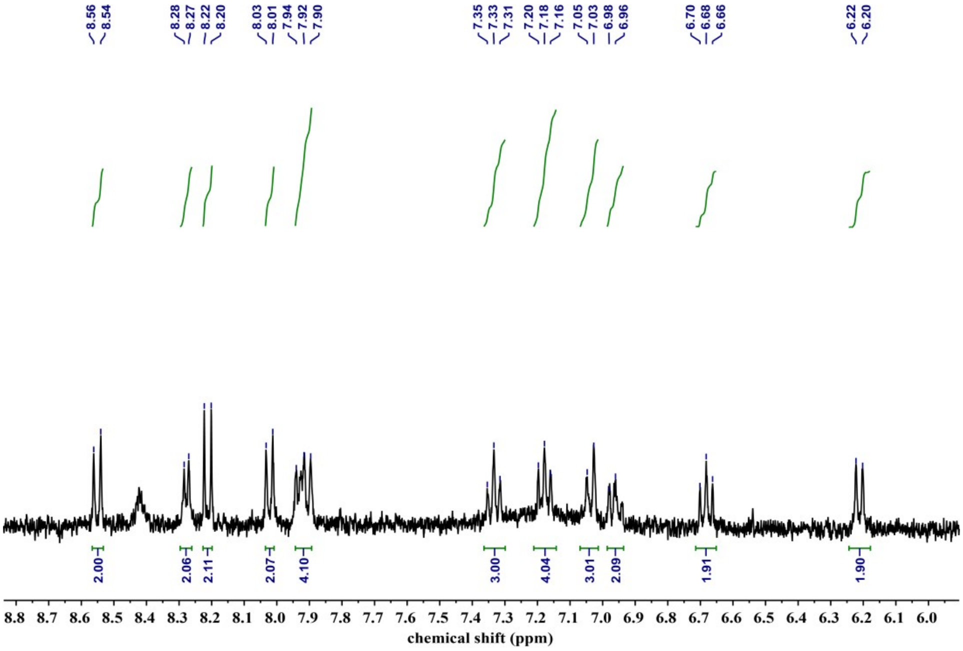

Figure S5. ^{1}H NMR (400 MHz, DMSO-d6) spectrum of Ir-COOH.

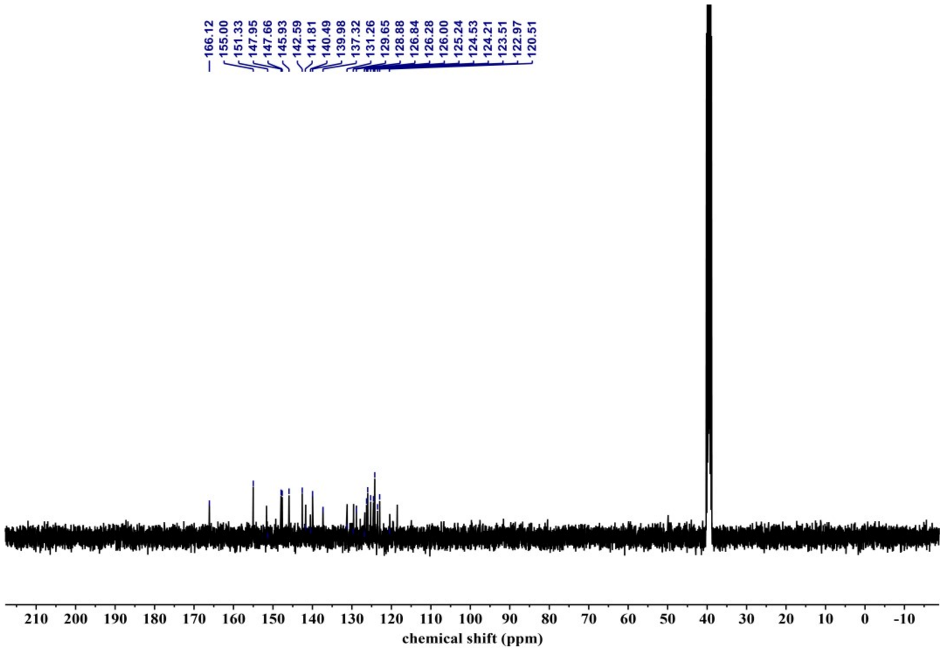

Figure S6. ^{13}C NMR (101 MHz, DMSO-d6) spectrum of Ir-COOH.

For the synthesis of Ir-Bpy and Ir-Phen, 2,2'-bipyridine or 1,10-phenanthroline was used instead of [2,2'-bipyridine]-4,4' -dicarboxylic acid and other conditions were consistent.

Ir-Bpy: ^{1}H NMR (400 MHz, DMSO-d6) δ 8.56 (d, J = 8.7 Hz, 2H), 8.40 (d, J = 8.0 Hz, 2H), 8.32 (d, J = 4.1 Hz, 2H), 8.21 (d, J = 8.6 Hz, 2H), 8.11 (t, J = 8.6 Hz, 2H), 8.00 (d, J = 8.1 Hz, 2H), 7.91 (d, J = 8.1 Hz, 2H), 7.75 (t, J = 7.3 Hz, 2H), 7.34 (dt, J = 8.0, 3.6 Hz, 2H), 7.19 – 7.10 (m, 2H), 6.97 (d, J = 3.9 Hz, 4H), 6.67 (t, J = 8.2 Hz, 2H), 6.22 (d, J = 8.2 Hz, 2H). ^{13}C NMR (101 MHz, DMSO-d6) δ 166.55, 155.44, 152.06, 148.38, 148.08, 146.37, 143.03, 142.11, 140.92, 140.42, 131.63, 129.27, 127.13, 126.70, 126.43, 125.67, 124.95, 124.62, 123.90, 123.39, 118.92. HRMS (ESI, m/z): $C_{44}H_{28}IrN_4S_2^+$, 869.14 [M]$^+$; found, 869.1346 [M]$^+$.

Ir-Phen: ^{1}H NMR (400 MHz, DMSO-d6) δ 8.78 – 8.69 (m, 4H), 8.49 (d, J = 8.7 Hz, 2H), 8.24 (d, J = 8.6 Hz, 2H), 8.11 (dd, J = 8.2, 5.3 Hz, 2H), 8.04 (d, J = 8.1 Hz, 4H), 7.77 (d, J = 9.7 Hz, 2H), 7.17 (q, J = 8.0 Hz, 4H), 6.89 (d, J = 8.9 Hz, 2H), 6.76 – 6.66 (m, 4H), 6.32 (d, J = 8.2 Hz, 2H). ^{13}C NMR (101 MHz, DMSO-d6) δ 151.48, 148.71, 148.07, 146.09, 145.67, 142.65, 141.53, 140.17, 139.48, 130.85, 130.14, 129.33, 127.91, 127.26, 126.70, 126.10, 125.69, 125.39, 124.55, 123.50, 122.39, 118.56. HRMS (ESI, m/z): $C_{46}H_{28}IrN_4S_2^+$, 893.14 [M]$^+$; found, 893.1366 [M]$^+$.

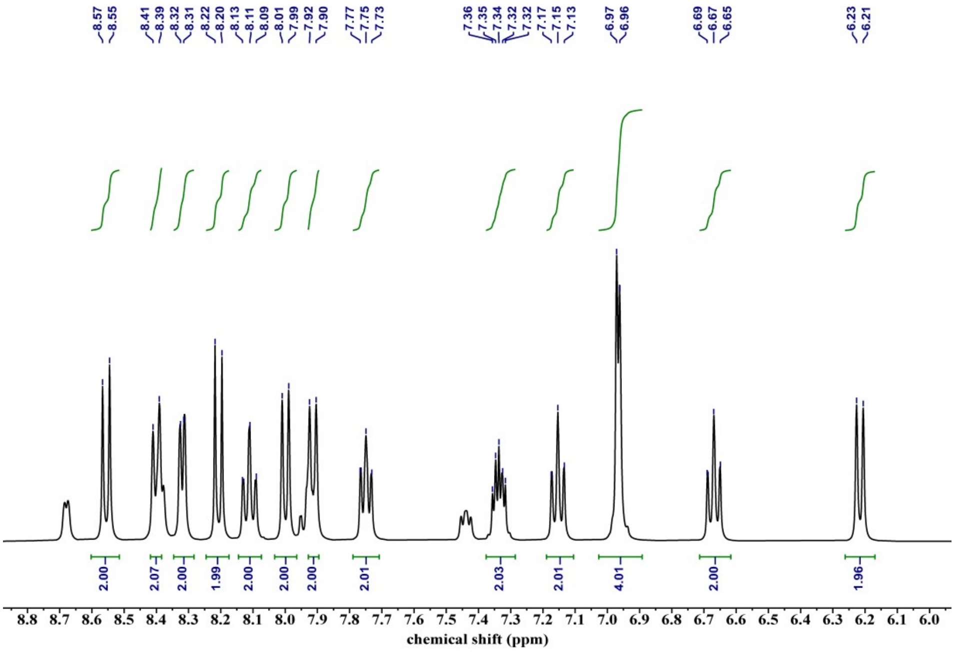

Figure S7. ^{1}H NMR (400 MHz, DMSO-d6) spectrum of Ir-Bpy.

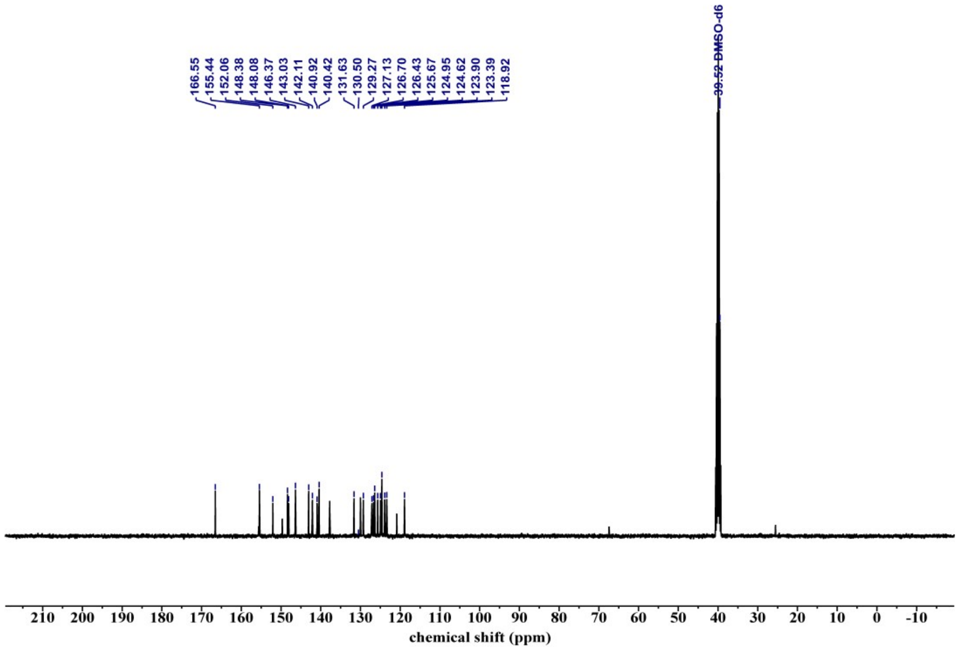

Figure S8. ^{13}C NMR (101 MHz, DMSO-d6) spectrum of Ir-Bpy.

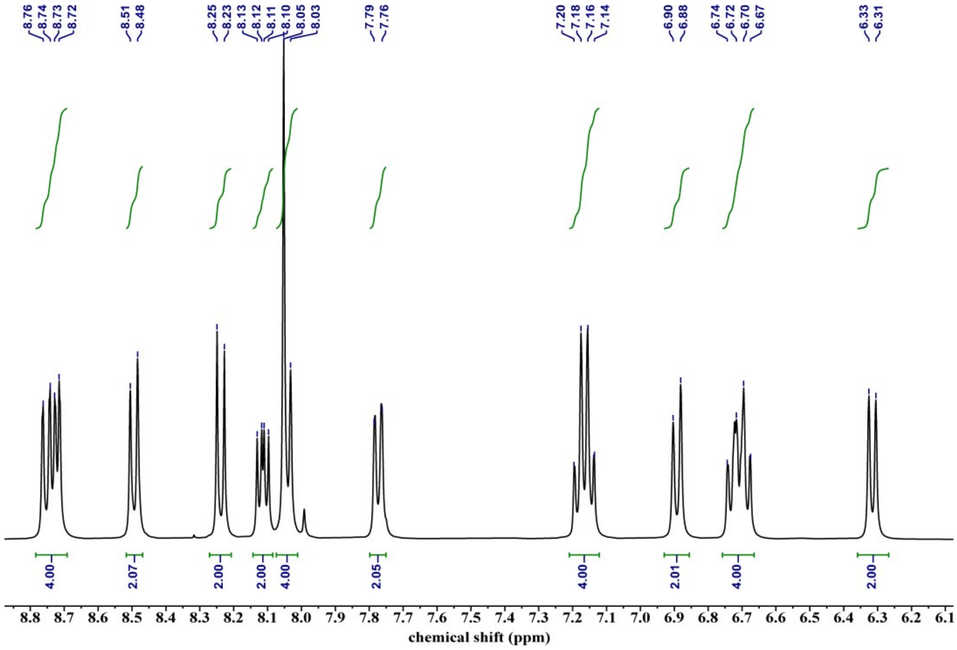

Figure S9. ^{1}H NMR (400 MHz, DMSO-d6) spectrum of Ir-Phen.

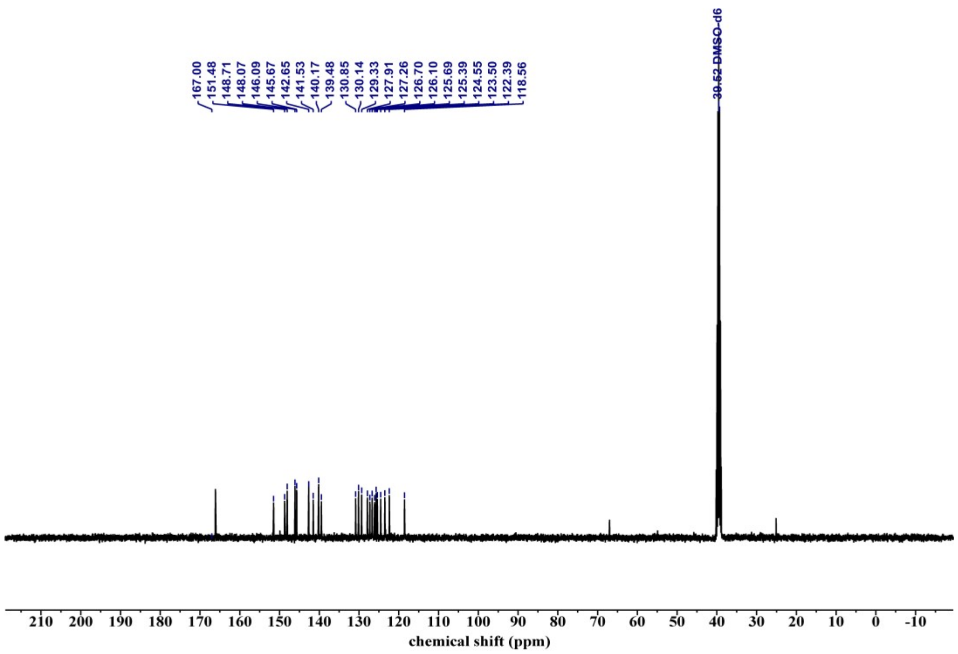

Figure S10. ^{13}C NMR (101 MHz, DMSO-d6) spectrum of Ir-Phen.

1.4 Preparation of Au NPs and SWCNTs-Au.

Au NPs was synthesized through a one-step reduction by sodium citrate[2]. Briefly, 60 mL ultrapure water was mixed with 500 μL 2% $HAuCl_4$ in a three necked flask and was heated to boiling under refluxing for 30 min with vigorous stirring. Then, 2 mL of 1% (w/v) sodium citrate was rapidly injected into the flask and was kept boiling for another 90 min. The obtained purple red solution was cooled to room temperature and stored at 4°C for further use.

10 mg SWCNTs was weighed and added to 5 mL of the above-mentioned Au NPs solution. The mixture was sonicated for about 20 min until the supernatant was colorless, centrifuged at 5000 rpm for 8 min, the precipitate was washed with ultrapure water and dried in vacuum at 60 °C overnight, denoted as SWCNTs-Au.

1.5 Measurement Procedure.

A conventional three-electrode system was used with the modified glassy carbon electrode (GCE, Φ = 3 mm) as working electrode, a platinum wire as counter electrode and Ag/AgCl (saturated KCl) as the reference electrode. The photomultiplier tube (PMT) was generally biased at 800 V, unless mentioned otherwise.

EIS measurements were executed in 0.1 M PBS solution containing 5 mM $K_3[Fe(CN)_6]/K_4[Fe(CN)_6]$ and 0.1 M KCl. The open potential was set at 0.22 V and the frequency range was from 0.01 Hz to 100 kHz with an alternating current amplitude of 5 mV.

1.6 Preparation of Modified Electrode.

Ir-COOH/GCE: different concentrations of Ir-COOH solution (dissolved in PBS:ethanol = 1:1, v:v) were mixed with 0.5% Nafion solution (100 μL 5% Nafion stock solution was diluted with 400 μL ethanol and 500 μL deionized water) at a ratio of 9:1. The mixture was sonicated for 20 min to mix evenly, and 3 μL was dropped onto the surface of the bare GCE and kept at room temperature until dry to form a uniform film.

Ir-COOH-SWCNTs/GCE: a certain amount of SWCNTs was added to the mixture of Ir-COOH and Nafion mentioned above, and the concentration of SWCNTs was 0.5 mg/mL. After ultrasonication for 20 min, 3 μL mixture was dropped on the surface of GCE and dried naturally to obtain Ir-COOH-SWCNTs/GCE.

Ir-COOH-Au NPs/GCE: compared with the preparation of Ir-COOH/GCE, this modified electrode has one more step of Au NPs modification. First, 5 μL of Au NPs prepared above was dropped on the surface of GCE. After drying at room temperature, 3 μL of the mixture of Ir-COOH and Nafion was added.

Ir-COOH-SWCNTs-Au/GCE: consistent with the preparation process of Ir-COOH-SWCNTs/GCE, except for replacing SWCNTs with SWCNTs-Au.

1.7 Detection Procedures of CAP.

The modified electrode Ir-COOH-SWCNTs-Au/GCE was immersed in 4 mL of PBS solution (0.1 M, pH 7.4) containing 10 mM $K_2S_2O_8$ as the coreactant and different concentrations of CAP to obtain ECL responses. The voltage of the PMT was set at 800 V. The ECL signal was recorded in the range of 0 to -1.1 V with a scan speed of 0.1 V/s.

1.8 Pretreatment of the Real Sample.

The milk and honey samples were obtained from a local supermarket. The milk sample (1 mL) was thoroughly mixed with acetonitrile (1 mL) and after a pause of 30 min, the mixture was centrifuged at 10,000 rpm for 5 min. The resulting supernatant was collected and diluted 10 times with ultrapure water for analysis. The pre-treatment process for honey sample involved dissolving 1 g of honey in 10 mL of ultrapure water and filtered it through a 0.45 μM membrane. For river water sample, it was taken from Jinjiang River (Chengdu, China) and then filtered via a 0.45 μM membrane for future use. Different amounts of CAP standard solution were added to the pretreated samples for the calculation of sample recovery rates.

2. Results and Discussion

2.1 The FT-IR Spectrum and PLQY of as-prepared Ir Complexes.

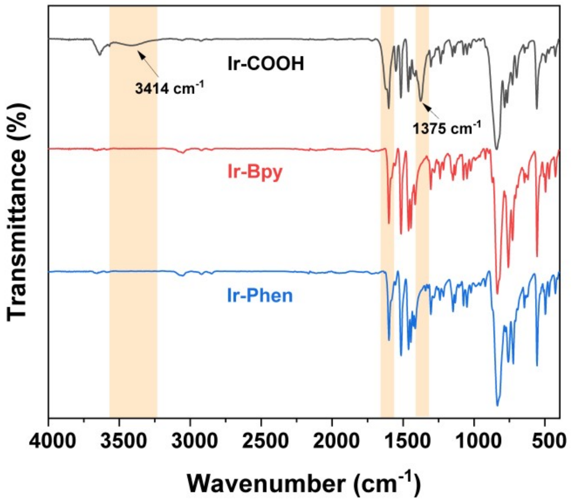

Figure S11. The FT-IR spectrum of as-prepared Ir-COOH, Ir-Bpy and Ir-Phen.

The FT-IR spectrum provides clear evidence for the presence of carboxyl groups (-COOH). A broad absorption band centered at 3414 cm^{-1} is observed, which is characteristic of the O-H stretching vibration. Additionally, a sharp absorption peak at 1375 cm^{-1} corresponds to the C-O stretching vibration of the carboxyl moiety. Compared with Ir-Bpy and Ir-Phen, the difference in the peak shape of Ir-COOH near 1700 cm^{-1} may be attributed to the C=O stretching vibration. These spectral features collectively confirm the existence of the carboxyl functionality.

The PLQY tests show that Ir-COOH, Ir-Bpy and Ir-Phen have almost identical PL quantum yield under the same experimental conditions. This suggests that their intrinsic radiative-to-nonradiative transition ratios are comparable. This also supports the conclusion from the side that the excellent ECL performance of Ir-COOH comes from the enhanced water solubility imparted by the carboxyl group.

Table S1. Absolute PL quantum yields of three Ir complexes.

Ir(III) complex	Ir-COOH	Ir-Bpy	Ir-Phen
ΦPL (%)	3.83	3.67	3.78

2.2 Annihilation ECL Behavior of Three Ir Complexes.

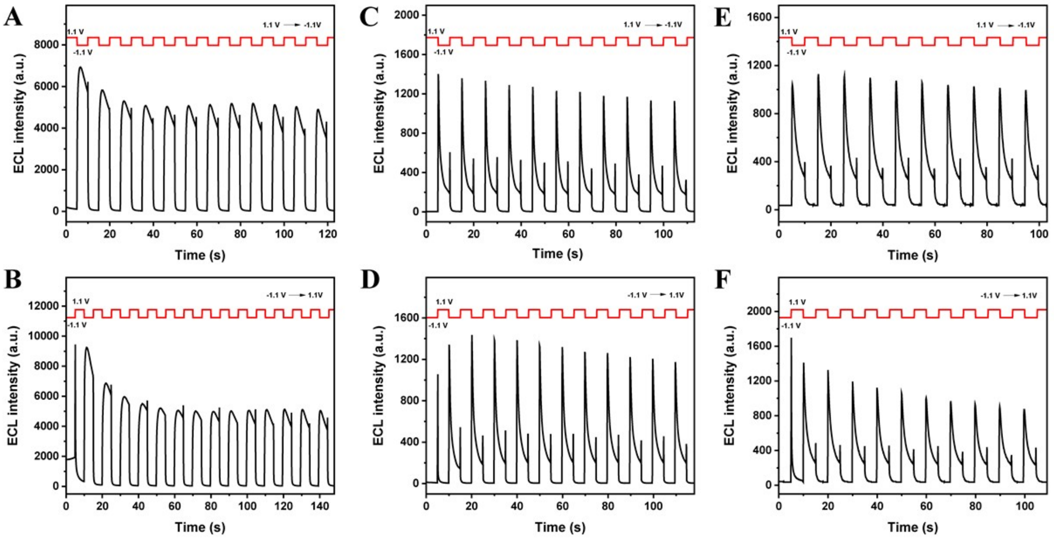

Figure S12. ECL annihilation test using step pulse voltammetry in PBS buffer (0.1 M, pH 7.4) with anodic scanning (1.1 V) for 5 s and cathodic (-1.1 V) scanning for 5 s. (A, B) Ir-COOH, (C, D) Ir-Bpy, (E, F) Ir-Phen.

The annihilation ECL of three Ir(III) complexes were further tested. During the step pulse test from 1.1 V to -1.1 V, the annihilation ECL of Ir-COOH were observed both when the potential switched from 1.1 V to -1.1 V and -1.1 V to 1.1 V (Figure S12A). However, when the potential was switched from 1.1 V to -1.1 V, the ECL maintained a strong ECL signal under the 5s pulse of -1.1 V. But when the potential was switched from -1.1 V to 1.1 V, the ECL signal decayed rapidly, indicating that the cationic radicals generated at 1.1 V had stronger stability[3-5]. When the cathode scan was preferred (Figure S12B), only rapidly decaying cathodic ECL was produced during the first voltage switch, and the dual-potential annihilation ECL appeared when the voltage was switched from 1.1 V to -1.1 V in the second round. These results show that the oxidation/reduction intermediates of Ir-COOH both have strong stability to produce double potential emission, but the oxidation intermediates produced at positive potential have relatively high stability. For Ir-Bpy and Ir-Phen, except that their dual-potential annihilation ECL all decays rapidly, they have annihilation ECL performance similar to Ir-COOH, but their ECL intensity and stability are significantly weaker than Ir-COOH.

2.3 The Electrochemical Properties of Three Ir Complexes.

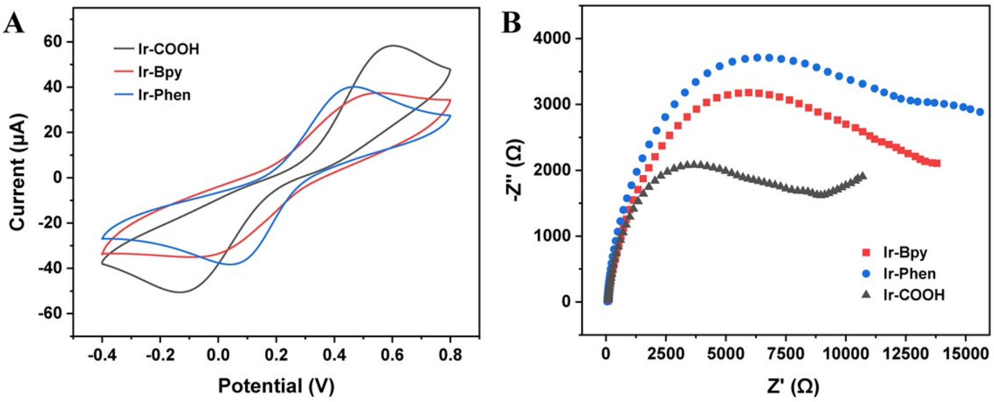

Figure S13. (A) CV and (B) EIS characterization of different Ir complexes modified electrode.

CV and EIS tests have been employed to monitor the interface properties of different Ir complexes modified electrodes. The Nyquist chart consists of a semicircular part in the higher frequency range and a straight part in the lower frequency range. The diameter of the semicircle is equal to the electron transfer resistance (Ret) at the electrode interface and related to the difficulty of electron transfer of a ferricyanide-redox probe between the electrode and the solution[6]. CV test in Figure S13A show that Ir-COOH has a higher redox peak current and slightly increased peak potential separation (ΔEp) than Ir-Bpy and Ir-Phen. At the same time, EIS characterization results in Figure 13B show that Ir-COOH has the lowest Ret. The above results indicate that the Ir complex in the Ir-COOH modified electrode forms a more uniform modification layer on the electrode surface to increase the effective active area[7].

2.4 ECL Efficiency Calculation.

The ECL efficiency is defined as the number of photons transmitted per electron. The relative ECL efficiency of the Ir-COOH/$K_2S_2O_8$ was evaluated by comparing the ratio of generated photons to consumed electrons, using the $Ru(bpy)_3^{2+}/K_2S_2O_8$ couple as the reference, which was calculated using the following equation[8]:

$$\Phi_x = \frac{\left(\frac{\int_0^t Idt}{\int_0^t idt}\right)_x}{\left(\frac{\int_0^t Idt}{\int_0^t idt}\right)_{st}} \times 100\%$$

Here, x represents the ECL emitter Ir-COOH while st stands for standard $Ru(bpy)_3^{2+}$, and I and i represent the ECL intensity and the corresponding current value under the same conditions, respectively. The potential was cycled between 0 V and -1.1 V with a scan rate of 100 mV/s by cyclic voltammogram in 0.1 M PBS (pH 7.4) containing 10 mM $S_2O_8^{2-}$. The PMT was biased at 800 V.

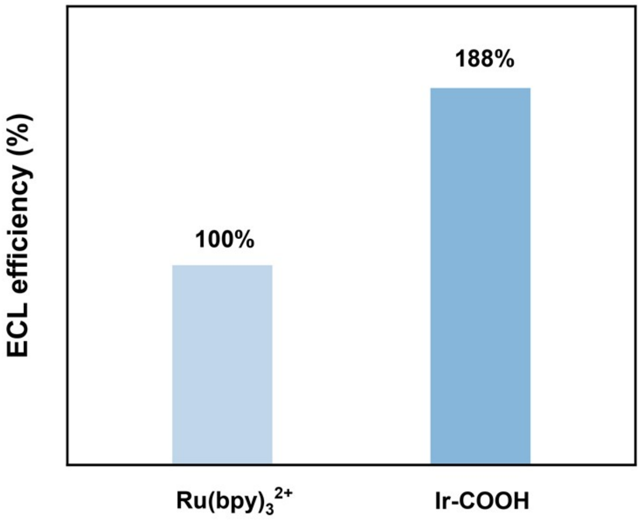

Figure S14. Relative ECL efficiency of $Ru(bpy)_3^{2+}$ and Ir-COOH.

Table S2. Comparison of the ECL efficiency (ΦECL) of different luminophors.

Luminophors	**Coreactants**	**ΦECL***	**References**
$\mathrm{Bis_{LT}}$-Ir-NHC	TPA	68.4%	[9]
$\mathrm{Ir(ppy)_2(napphen)^+}$	TPA	89%	[10]
$\mathrm{Ir(bpy\text{-}Me)_2(bpy\text{-}tBu)^{3+}}$	TPA / $K_2S_2O_8$	26% / 120%	[11]
$\mathrm{Ir@SiO_2}$	TPA	51.4%	[12]
IrCHO	TPA	16%	[13]
Ir-COOH	$K_2S_2O_8$	188%	This work

*ΦECL was calculated using $\mathrm{Ru(bpy)_3^{2+}}$ (ΦECL = 100%) as a reference under the same experimental conditions.

2.5 Optimization of the Experimental Conditions of Anodic ECL.

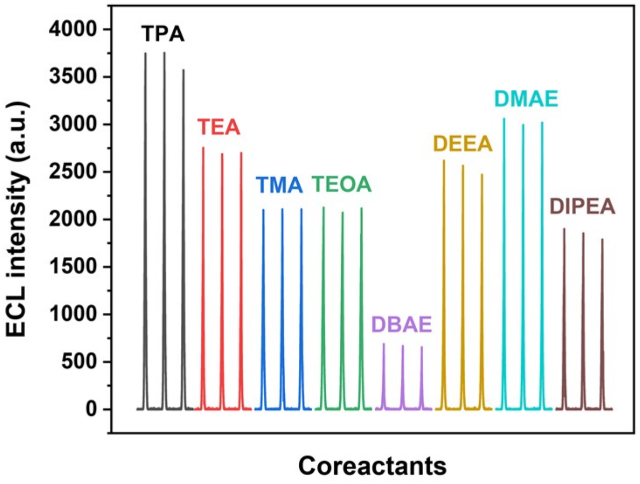

Figure S15. ECL intensity of Ir-COOH/GCE in 0.1 M PBS (0.1 M, pH 7.4) solution containing 10 mM of different anodic coreactants. Scan rate: 0.1 V/s, PMT: 850 V.

The anodic ECL performance of Ir-COOH was tested by using ubiquitous different coreactants including TPA, TEA, TMA, TEOA, DBAE, DEEA, DMEA and DIPEA. Among them, the Ir-COOH/TPA system showed the highest ECL intensity. In addition, when N_2H_4 or NaC_2O_4 was used as coreactant, there was almost no ECL signal in the system. Thus, TPA was selected as the optimized coreactant for the ECL of Ir-COOH in subsequent experiments of this study.

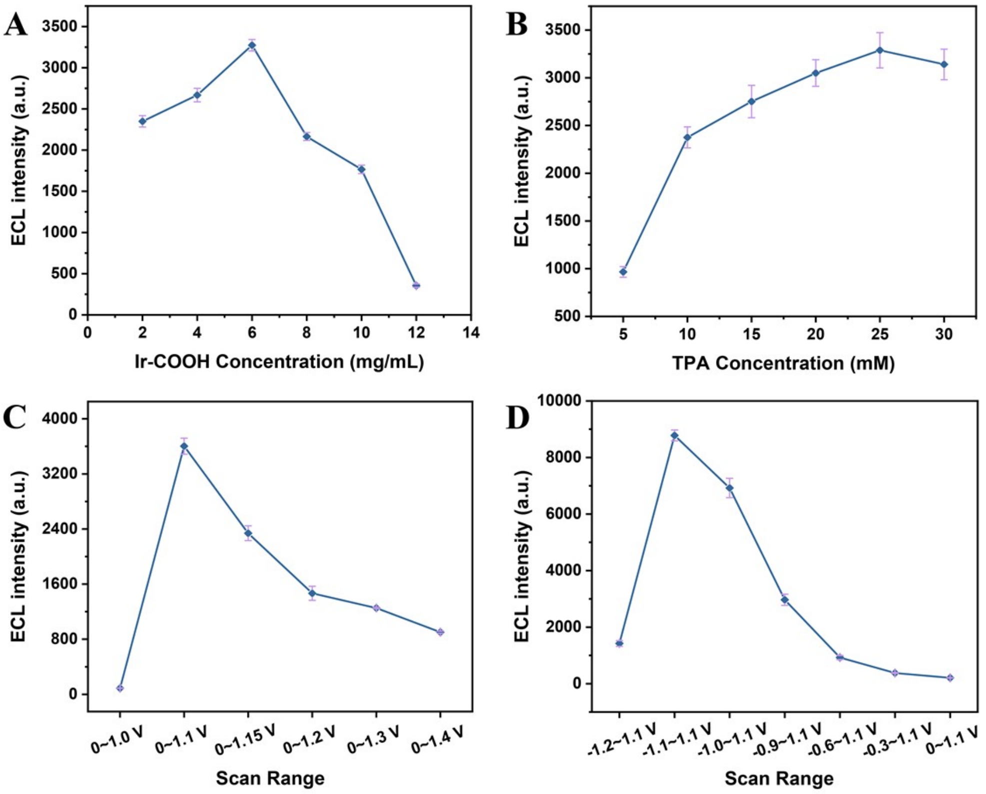

Figure S16. Effects of (A) concentrations of the Ir-COOH, (B) concentrations of the TPA, and (C, D) scanning potential on ECL intensity of Ir-COOH/TPA system. Error bars, SD, n = 3.

To achieve an optimal ECL performance, several experiment conditions were investigated. Firstly, the concentrations of the Ir-COOH were investigated and the corresponding results were displayed in Figure S16A. It was observed that the ECL response was increased with the concentration of the Ir-COOH and then decreased after 6 mg/mL. Thus, the optimal concentration of the Ir-COOH of 6 mg/mL was selected in the following experiments. Then, Figure S16B plotted the change of the ECL signals with the concentrations of the TPA. With the concentration increased from 5 to 20 mM, the ECL signal continually increased. When the concentration was more than 20 mM, the ECL signal was almost unchanged, suggesting that the optimal concentration of the TPA was 20 mM.

Next, according to Figure S16C, when the scanning window was 0 ~ 1.0 V, the ECL signal was close to 0 a.u., which was due to the fact that the oxidation potential of Ir-COOH is not reached. When it was scanned from 0 to 1.1 V, there was the strongest signal value. However, when the scanning range was further expanded to the more positive potential, the ECL intensity decreased continuously. This may be due to the short life of the oxidation intermediate product, the longer the scanning time, the more the consumption. The use of a negative potential to restore those oxidizing substances back to their precursor molecules through an electrochemical reduction process can enhance the luminescence intensity[14]. As shown in Figure S16D, when the lowest negative potential of -1.1 V was employed, ECL intensity of Ir-COOH/TPA syetem reached its maximum. Therefore, -1.1 to 1.1 V was chosen as the optimal scanning potential range of anode ECL test.

2.6 ECL Mechanism.

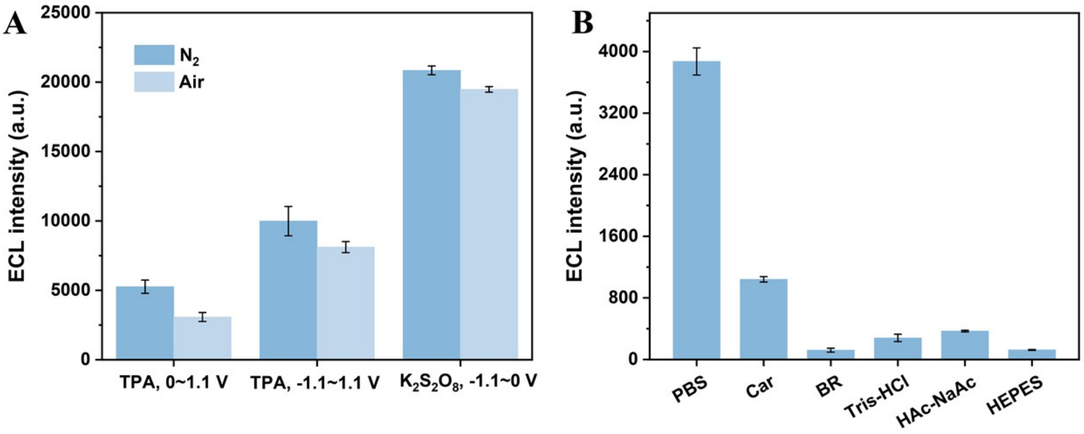

Figure S17. ECL response of (A) Ir-COOH modified GCE with air and saturated N_2 in PBS containing TPA or $K_2S_2O_8$ and (B) Ir-COOH/GCE in different buffer systems.

The effect of dissolved oxygen on ECL intensity was examined, as shown in Figure S17A for cathodic ECL, the ECL intensity of the N_2 saturated group and the control air saturated group was basically unchanged, and the effect of dissolved oxygen could be excluded. For the anodic luminescence of the Ir-COOH/TPA system, the ECL intensity was enhanced after the elimination of dissolved O_2 by N_2, which may be due to the fact that TPA with poor water solubility was more evenly dispersed in PBS during the process of drum N_2, which was more conducive to electrooxidation near the electrode to enhance luminescence. These results showed that dissolved oxygen could not affect the ECL response of Ir-COOH.

The electrolyte solution is an important component of ECL systems because it can affect ECL. In Figure S17B, we compared the ECL of Ir-COOH in different buffer systems including PBS, carbonate (Car), borate buffer (BR), Tris-HCl buffer, acetate buffer (HAc-NaAc) and HEPES buffer, all buffers were 0.1 M, pH 7.4. The results showed that modified electrode Ir-COOH/GCE had the strongest ECL in PBS buffer, so PBS was selected as the electrolyte solution of this experiment.

2.7 Characterization of the Prepared Au NPs and SWCNTs-Au.

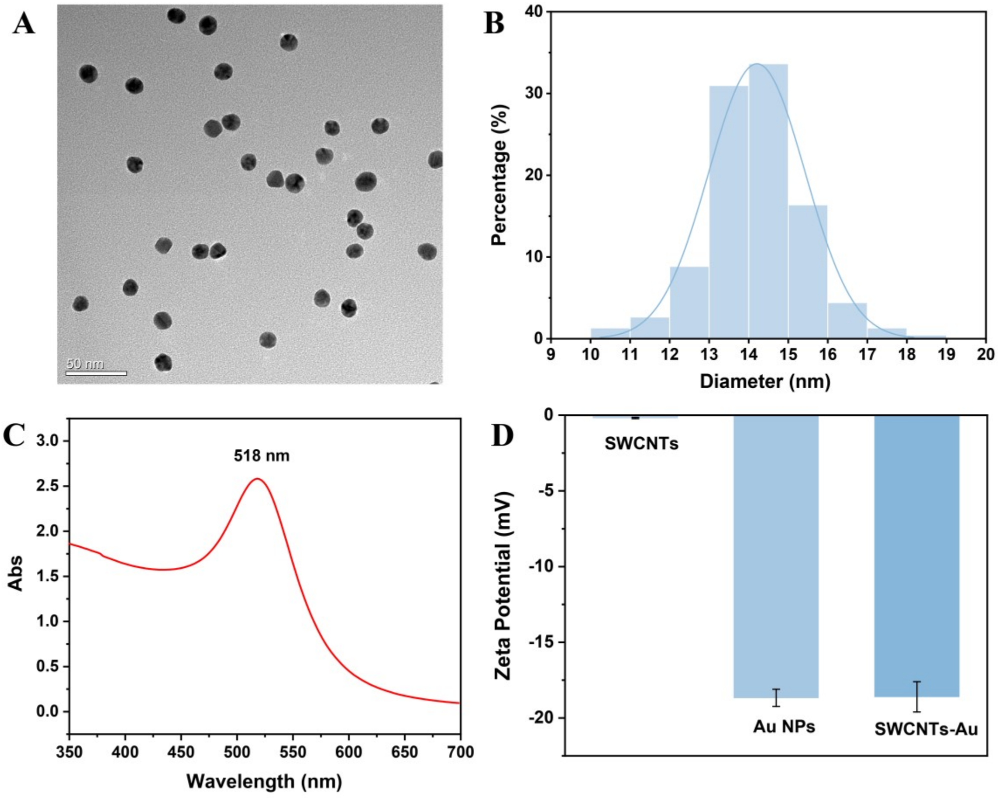

Figure S18. (A) TEM image of Au NPs. (B) Size distribution of Au NPs. (C) UV-Vis spectrum of Au NPs. (D) Zeta potential of SWCNTs, Au NPs and SWCNTs-Au.

As shown in Figure S18, the size of Au NPs were about 14 nm, and the morphology and size of Au NPs were homogeneous. The corresponding UV-Vis absorption wavelength of 14 nm Au NPs was located in 518 nm (Figure S18), which was consistent with the literature report[15]. The binding of the SWCNTs to Au NPs was characterized by Zeta potential measurements (Figure S18), SWCNTs was almost electrically neutral, but SWCNTs-Au had a negative potential close to that of Au NPs, indicating the success of Au NPs modification.

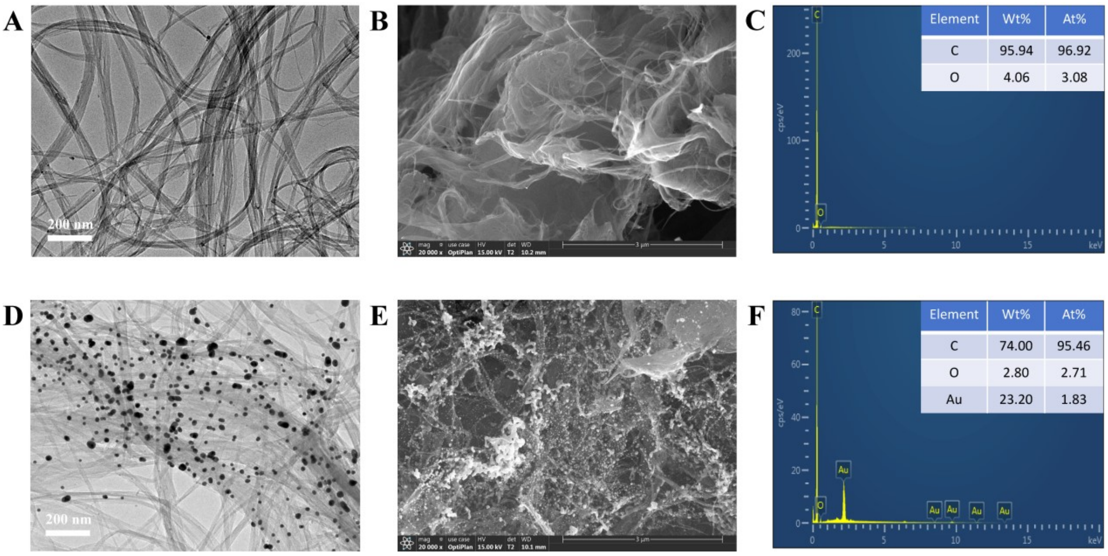

Figure S19. TEM image of (A) SWCNTs and (D) SWCNTs-Au. SEM image and EDS spectrum of SWCNTs (B, C) and SWCNTs-Au (E, F).

In Figure S19A, well-dispersed single nanotubes and aggregated bundles can be seen at the same time. As shown in Figure S19D, the microstructure of SWCNTs-Au was that a large number of Au NPs were attached to the crisscross SWCNTs, but the size of Au NPs was not uniform due to the adsorption and agglomeration caused by the ultrasonic process, which was inconsistent with the characterization of the as prepared monodisperse Au NPs (Figure S18). Figure S19B shows the SEM image of SWCNTs. From the morphology, it is observed that the sample was interwoven by a large number of slender and meandering one-dimensional nanostructures, forming a highly porous and continuous network structure. Compared to pristine SWCNTs, it can be clearly seen in Figure S19E that there were both monodisperse and agglomerated Au nanoparticles loaded on the fibrous tubular SWCNTs. Furthermore, the elemental composition of SWCNTs-Au was investigated by using energy-dispersive X-ray spectroscopy (EDS). Compared to that of SWCNTs which containing only C and O elements (Figure S19C), the EDS analysis in Figure S19F revealed a 1.83% presence of Au elements in SWCNTs-Au, further confirming the successful incorporation of the Au element.

2.8 Characterization of the Stepwise Modified Electrode.

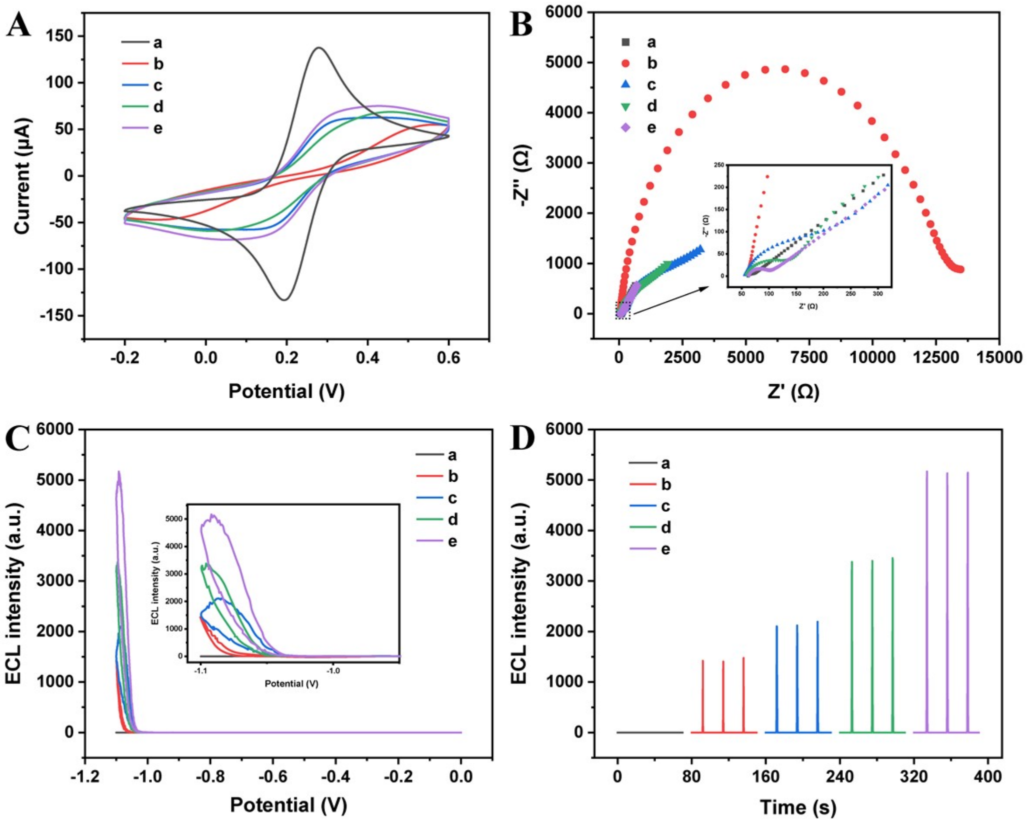

Figure S20. (A) CV, (B) EIS and (C, D) ECL characterization of the stepwise modified electrode. (a) bare GCE, (b) Ir-COOH/GCE, (c) Ir-COOH-SWCNTs/GCE, (d) Ir-COOH-Au NPs/GCE, and (e) Ir-COOH-SWCNTs-Au/GCE.

As presented in Figure S20C and S20D, almost no ECL signal was observed for the bare GCE (curve a). After the immobilization of the Ir-COOH, an enhanced ECL signal could be obtained (curve b) owing to the excellent ECL performance of the Ir-COOH. The ECL signal increased once again (curve c) with the Ir-COOH-Au NPs modified GCE on account of the outstanding conductivity of Au NPs. When Ir-COOH-SWCNTs were dropped on the GCE surface, the ECL signal also significantly enhanced (curve d), this may be attributed to the good conductivity of SWCNTs, which accelerated the electron transfer of Ir-COOH. Secondly, the Ir-COOH-SWCNTs composite modified electrode increased the specific surface area due to the mesoporous properties of SWCNTs, which enhanced the diffusion of the coreactant $K_2S_2O_8$ in the electrolyte and the reduction of the electrode surface. And Ir-COOH-

SWCNTs-Au/GCE possessed the strongest ECL intensity (curve e) due to the synergistic effect of SWCNTs and AuNPs.

CV and EIS tests have been employed to monitor the interface properties of different modified electrodes to clarify the enhancement mechanism of the nanomaterials to ECL. Firstly, as shown in Figure S20A and S20B, the bare GCE showed a well-defined characteristic redox peak of $[Fe(CN)_6]^{3-}/[Fe(CN)_6]^{4-}$ and a very small semicircle was acquired from the EIS response (curve a), while the Ir-COOH/GCE showed a remarkably decreased peak current and an turgidly increased Ret response due to the modification of Ir-COOH on GCE surface formed a layer that can hinder the access of the soluble $[Fe(CN)_6]^{3-/4-}$ redox probe to the electrode surface (curve b). When Ir-COOH-SWCNTs or Ir-COOH-Au NPs were coated on the GCE, it can be seen that compared with the curve b, the curves c and d had evidently reduced ΔE_p, higher peak current (i_p) and decreased Ret response because of the excellent conductivity of AuNPs and SWCNTs. And after Ir-COOH-SWCNTs-Au was modified on the electrode surface, the peak current further increased and Ret value closer to the bare GCE. All these results indicated that the nanomaterials enhanced the ECL intensity by accelerating the electron transfer on the electrode surface.

2.9 Optimization of Experimental Conditions.

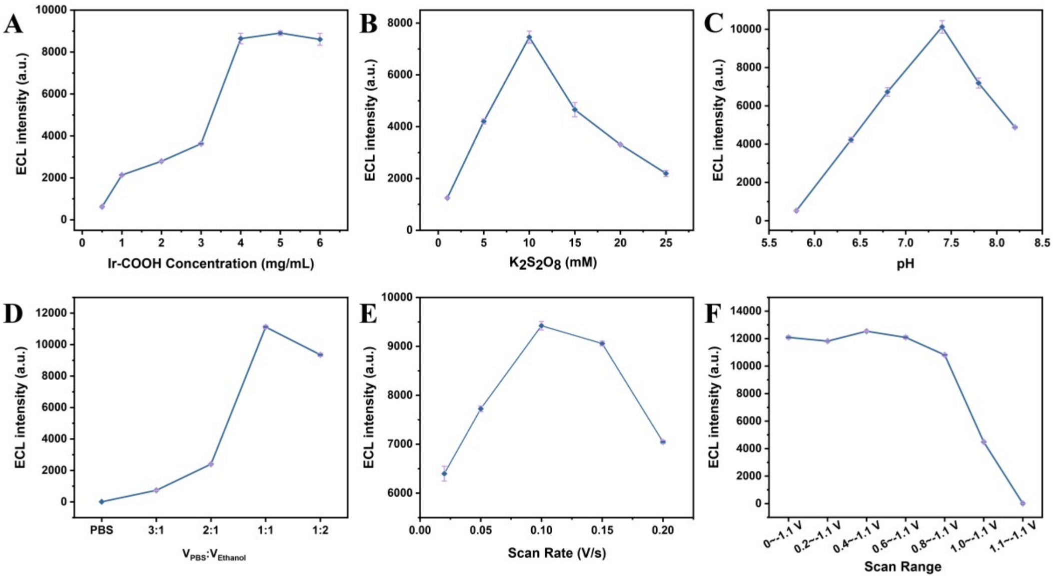

Figure S21. Effect of (A) concentration of Ir-COOH, (B) concentration of $K_2S_2O_8$, (C) pH, (D) the solvent ratio of PBS:ethanol (v:v) for preparing Ir-COOH solution for the preparation of Ir-COOH/GCE, (E) scan rate and (F) scanning potential on ECL intensity.

As the luminophore, the concentrations of Ir-COOH were closely associated with the ECL intensity, which were first investigated and the corresponding results were displayed in Figure S21A. With the concentration increased from 1 mg/mL to 4 mg/mL, the ECL signal continually increased. When the concentration was more than 4 mg/mL, the ECL signal changed slowly, suggesting that the optimal concentration of the Ir-COOH was 4 mg/mL. Then, Figure S21B plotted the change of the ECL signals with the concentrations of the $K_2S_2O_8$. It was observed that with the increasing $K_2S_2O_8$ concentration, the ECL signal of Ir-COOH gradually intensified, reaching its peak at 10 mM. However, further increasing the $K_2S_2O_8$ concentration resulted in a decline in the ECL signal. Thus, the optimal concentration of the $K_2S_2O_8$ of 10 mM was selected in the following experiments. In addition, the pH dependence on this ECL system was also investigated (Figure S21C). The ECL signal reached maximum when pH is 7.4, and when the pH value continued to increase, the ECL intensity decreased rapidly. The dissolution state of the luminophore had an important effect on its ECL intensity. So, the solvent ratio of PBS:ethanol (v:v) for preparing Ir-COOH solution were also optimized. Due to the poor solubility of Ir-COOH in PBS, the surface of the modified electrode was extremely uneven, and the ECL signal was close to 0. With the increase of ethanol ratio in the solvent, the solubility of Ir-COOH increased with the increase of ECL intensity, and the strongest ECL was observed when PBS:ethanol = 1:1 (v:v) (Figure S21D).

In addition, we considered the effect of electrochemical parameters on the ECL of the system. We optimized the scan rate to 0.1 V/s, as shown in Figure S21E, the ECL intensity increased when the scan rate increased from 0.02 V/s to 0.1 V/s, but when the scan rate continued to increase, the ECL intensity decreased instead, which may be due to the mismatch between the formation of luminogen ions and the diffusion rate of the coreactant $K_2S_2O_8$ to the electrode surface. Finally, the effect of the scanning potential window on the ECL intensity was also investigated (Figure S21F). When the scanning potential was only negative, Ir-COOH/$K_2S_2O_8$ system had the strongest luminescence when scanned from 0 to -1.1 V. When the scanning window was further expanded to positive from 0 ~ -1.1 V to 0.8 ~ -1.1 V, the ECL intensity was almost unchanged. However, due to the oxidation potential of Ir-COOH was reached by increasing the scanning interval to 1.0 ~ -1.1 V or 1.1 ~ -1.1 V, the consumption of Ir-COOH caused by anodic oxidation led to a sharp decrease in cathodic ECL. Therefore, in order to meet both strong ECL intensity and short scanning time, the 0 ~ -1.1 V was selected as the optimal scanning range and was applied to the subsequent experiments.

2.10 The Quenching Mechanism of ECL by CAP.

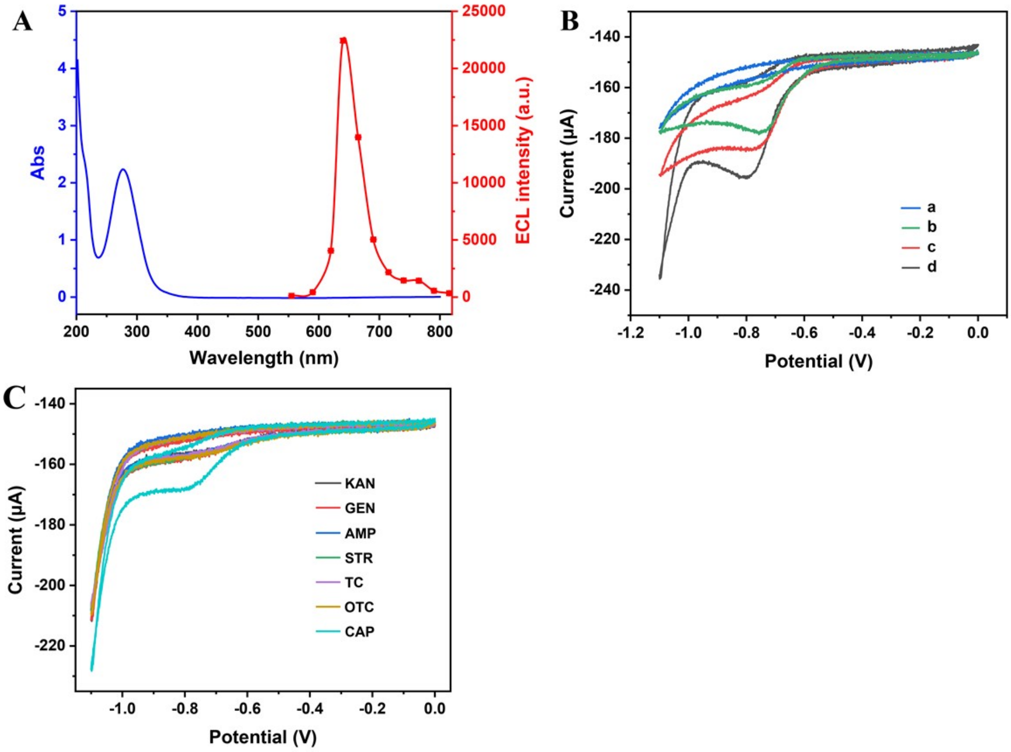

Figure S22. (A) UV-Vis absorption spectrum of CAP (blue) and ECL emission spectrum of Ir-COOH (red). (B) CV curves of Ir-COOH/$K_2S_2O_8$ with or without CAP, bare GCE + PBS containing $K_2S_2O_8$ (curve a), bare GCE + PBS + CAP (curve b), bare GCE + PBS containing $K_2S_2O_8$ + CAP (curve c), Ir-COOH/GCE + PBS containing $K_2S_2O_8$ + CAP (curve d). (C) CV curves of Ir-COOH/$K_2S_2O_8$ with different antibiotics.

As shown in Figure S22A, there had no spectral overlap between the UV-Vis absorption profile of CAP and the ECL emission profile of Ir-COOH in the 200 to 800 nm wavelength band, which excluded the luminescence quenching caused by resonance energy transfer (RET). Subsequently, the CV curves of different systems were recorded (Figure S22B). It was found that in the presence of CAP, there was an obvious reduction peak around -0.7 V, which could be inferred that the reduction process of CAP had an effect on ECL and led to the quenching of ECL signal[16]. At the same time, it can be seen in Figure S22C that other interfering substances did not show obvious reduction peaks during the CV scan of 0 ~ -1.1 V, which also indicated the source of specific detection of CAP.

2.11 Determination of CAP in Real Samples.

To evaluate the practical applicability of the constructed ECL sensor, spiked recovery experiments were conducted and different final concentrations of CAP (10, 20, and 50 μM) were spiked to the samples for detection. Baseline detection was first performed on raw milk, honey and river water samples that did not add CAP. The detection result indicated the absence of CAP in the real samples. As shown in Table S1, the recovery rates were 95.2 − 104.0, 95.5 − 100.6, and 94.7 − 107.1%, with average recoveries of 99.4, 97.7, and 101.8% (RSD < 5%), for milk, honey and river water, respectively. The analytical results demonstrated high sensitivity and reliability, thereby substantiating the good practicality in the CAP detection of real samples.

Table S3. Analytic results of CAP in various real samples.

Sample	Original content (μM)	Added (μM)	Found (μM)	Recovery (%)	RSD (%, n = 3)
Milk	0	10.00	9.91	99.1	1.80
		20.00	19.04	95.2	3.06
		50.00	52.00	104.0	2.04
Honey	0	10.00	9.69	96.9	3.68
		20.00	20.12	100.6	3.33
		50.00	19.10	95.5	1.49
River water	0	10.00	10.35	103.5	2.15
		20.00	18.94	94.7	1.87
		50.00	53.55	107.1	0.74

Table S4. Comparison of different methods for CAP detection.

Methods	Linear range	LOD	References
Electrochemistry (CV)	0.5-50 µM	66 nM	[17]
Electrochemistry (DPV)	10-331 µM	0.98 µM	[18]
Electrochemistry (CA)	0.05-100 µM	16 nM	[19]
Photoelectrochemistry	0.01-50 nM	4.12 pM	[20]
Mag. Solid-phase Microextraction (MSPME)-HPLC	0.004-0.2 mg/L	0.69 µg/L	[21]
ECL	0.5 pM-100 nM	0.12 pM	[22]
ECL	1-100 µM	0.82 µM	This work

CV (cyclic voltammetry), DPV (differential pulse voltammetry), CA (chronoamperometry)

Compared with the reported CAP sensors, although our sensor design is simple, the detection ability of our method needs to be further strengthened, and we hope to make a greater breakthrough in detection sensitivity. In the future, we will consider how to further optimize the sensing performance by combining biological amplification and other technologies while ensuring the simplicity of the sensing process.

References.

1. Y. Dai, Z. Zhan, L. Chai, L. Zhang, Q. Guo, K. Zhang and Y. Lv, *Anal. Chem.*, 2021, **93**, 4628-4634.
2. Z. Huang, X. Xie, Y. Wu, R. Liu and Y. Lv, *J. Am. Chem. Soc.*, 2025, **147**, 4904-4914.
3. W. Liang, M. Wang, C. Ma, J. Wang, C. Zhao and C. Hong, *Small*, 2024, **20**, 2306473.
4. C. Hu, H. Xiang, Y. Yin, J. Li, Y. Zhang, X. Huang, Y. Guo, Y. He, Y. Gao, K. Ren, H. Han, W. Wang and J. Li, *Analytical Chemistry*, 2025, **97**, 3153-3160.
5. W. Gu, X. Wang, M. Xi, X. Wei, L. Jiao, Y. Qin, J. Huang, X. Cui, L. Zheng, L. Hu and C. Zhu, *Analytical Chemistry*, 2022, **94**, 9459-9465.
6. Q. Hu, L. Su, Y. Mao, S. Gan, Y. Bao, D. Qin, W. Wang, Y. Zhang and L. Niu, *Biosensors and Bioelectronics*, 2021, **178**, 113010.
7. M. Schalenbach, V. Selmert, A. Kretzschmar, L. Raijmakers, Y. E. Durmus, H. Tempel and R.-A. Eichel, *Physical Chemistry Chemical Physics*, 2024, **26**, 14288-14304.

8. Y.-T. Yang, Y.-Z. Guo, Z.-C. Shen, J.-L. Liu, R. Yuan and Y.-Q. Chai, *Anal. Chem.*, 2023, **95**, 9314-9322.
9. C. Dai, Z. Mao, Y. Xu, J. Jia, H. Tang, Y. Zhao and Y. Zhou, *Analytical Chemistry*, 2024, **96**, 7311-7320.
10. W. Qu, X. Yang, X. Huang, W. Guo and Z. Dai, *Dalton Transactions*, 2024, **53**, 5284-5290.
11. S. J. Blom, T. U. Connell, E. H. Doeven, D. J. Hayne, E. Kerr, L. C. Henderson and P. S. Francis, *Journal of Electroanalytical Chemistry*, 2023, **933**, 117273.
12. Z. Mao, Y. Zhao, J. Dong, L. Li and Y. Zhou, *Sensors and Actuators B: Chemical*, 2023, **394**, 134480.
13. H. S. No and J.-I. Hong, *RSC Advances*, 2023, **13**, 32070-32076.
14. Y. Yang, H. Jiang, J. Li, J. Zhang, S.-Z. Gao, M.-L. Lu, X.-Y. Zhang, W. Liang, X. Zou, R. Yuan and D.-R. Xiao, *Mater. Horiz.*, 2023, **10**, 3005-3013.
15. J. Zhao, X. Tan, Y. He, R. Yuan, S. Wang and S. Chen, *Analytical Chemistry*, 2024, **96**, 6218-6227.
16. A. K. J, S. Reddy, S. Acharya, L. B, K. Deepak, C. S. Naveen, K. N. Harish and S. Ramakrishna, *Analytical Methods*, 2022, **14**, 3228-3249.
17. N. X. Dinh, T. N. Pham, T. Q. Huy, D. Q. Trung, P. A. Tuan, V. Q. Khue, N. Van Quy, V. P. Le, V. D. Lam and A.-T. Le, *New Journal of Chemistry*, 2021, **45**, 7622-7636.
18. M. Di-Oliveira, R. G. Rocha, L. V. de Faria, E. M. Richter and R. A. A. Munoz, *Journal of The Electrochemical Society*, 2022, **169**, 047517.
19. Z. Shi, L. Liu, X. Wu, Z. Ma, Y. Li, W. Sun, C. M. Li, H. B. Yang and C. X. Guo, *Talanta*, 2025, **289**, 127725.
20. F. Yu, M. Huang, R. Wang, C. Hao and Y. Zhu, *Biosensors and Bioelectronics*, 2025, **268**, 116917.
21. J. Zhang, Y. Ma, J. Cao, A. Li, S. Liu, X. Yang, L. Wang, J. Li and X. Hu, *Analytical Chemistry*, 2025, **97**, 19742-19758.
22. J. Yi, X. Dong, Y. Sun, X. Wang, X. Kuang, Y. Du, H. Ma, D. Fan, R. Feng and Q. Wei, *Analytical Chemistry*, 2025, **97**, 24815-24823.